8

significantly correlated to $BMRO_2$, as measured from the trachea gas sampling (Figure 4). The latter two parameters (k_w and p) appeared to be consistent and did not differ across various species (Table 2). Also, change in those parameters was less sensitive in $CMRO_2$ (Figure 1). These findings suggest that the production of RW after inhalation of $^{15}O_2$ could be described only by a single parameter of k, as shown in Figure 3, although further studies are required to validate this because the method was only tested in a group with small number of subjects of particular physiologic situation (under anesthesia) and has not been applied to different populations. It is also important to note that this parameter (k) estimated from the $BMRO_2$ (i.e., BM approach) provided $CMRO_2$, which was consistent with the trachea gas samplings shown in Figure 4, and that the obtained OEF values by the approaches of 4PF, 1PF, and BM applied in the present study were not significantly different to that by A–V difference approach as revealed by Bland–Altman analysis.

The simulation study also showed that the most sensitive parameter in $CMRO_2$ was the RW production rate constant, k, followed by Δt. It was therefore suggested that k could be determined with a single blood sampling procedure using the 1PF approach, in which other parameter values were determined and fixed from results from the 4PF approach. It was further showed that k could be obtained from the BM approach as determined from oxygen concentration in the expiration gas. Both 1PF and BM approaches appeared to be robustly useful in $^{15}O_2$ PET for assessing quantitative $CMRO_2$ and CBF in clinical studies.

It is important to note that k varies significantly depending on the physiologic status even in the same species, as seen in Figure 4. According to the simulation study in Figure 1, this variation causes nonnegligible errors in $CMRO_2$, if a constant k is used. Changes in k from 0.1 to 0.6 per min causes errors in $CMRO_2$ of $\pm 30\%$ in anesthetized monkeys. Results from clinical studies, however, showed the variation in k being less. As shown in Table 2, k for clinical patients was 0.129 ± 0.023 per min, and the coefficient of variation was approximately 18%. Previous work by Huang et al (1991) also showed similar value with comparable variations, namely 0.131 ± 0.026 per min in six human subjects. These variations caused only $\pm 5\%$ errors in $CMRO_2$, according to the simulation shown in Figure 1. The small variation in k in clinical patients is attributed to the fact that all subjects were studied at a relatively stable condition without physiologic stimulation. However, careful attention is needed if one intends to scan the patients whose whole-body oxygen metabolism is largely changed from the baseline condition. For example, during several pharmacologically stressed (Wessen et al, 1997; Kaisti et al, 2003), exercise-induced physically stressed, and hyper- or hypothermia (Sakoh and Gjedde, 2003) conditions.

The simulation also showed that size of errors in $CMRO_2$ increased in smaller animals, where the value of k was larger. Recently, $CMRO_2$ as well as CBF have been measured in rats using a small animal PET scanner (Magata et al, 2003; Yee et al, 2006). Magata et al performed multiple blood samplings and plasma separation for multiple blood samples to estimate the RW in their experiment involving rats. The procedures were crucial, but have caused serious alterations of physiologic condition in heart pressure and heart rate due to large amount of blood samples for small animals. Our proposed simplified technique for estimating RW from a single blood sample or from $BMRO_2$, is essential for small animals to be able to maintain the physiologic status. The calculation of $CMRO_2$ also requires whole arterial TAC, which can be obtained from arterial blood samplings and could change the physiologic condition. However, such blood sampling could also be avoided by an arterial–venous bypass (Weber et al, 2002; Laforest et al, 2005), by placing a probe in femoral artery (Pain et al, 2004), or by a noninvasive method (Yee et al, 2006).

Mintun et al (1984) has proposed a simple procedure for RW correction based on a linear interpolation for the bolus $^{15}O_2$ inhalation 60-secs PET scan. As shown in Figure 2, the RW curve is not linear particularly in smaller animals, and a systematic error may be caused or scan duration is limited. Ohta et al (1992) and other investigators (Ohta et al, 1992; Fujita et al, 1999; Vafaee and Gjedde, 2000; Okazawa et al, 2001a, b; Yamauchi et al, 2003; Mintun et al, 2002), however, have used a technique which does not take into account the RW contribution. Only initial short-period data, namely the 3 mins after the bolus inhalation of $^{15}O_2$, were used in their approach, and thus estimated parameters suffered from statistical uncertainties. The present methodology to estimate RW in the arterial blood allows the prolongation of a PET acquisition period. The technique can also be applicable to the recently proposed sequential administration protocol of $^{15}O_2$ followed by $H_2^{15}O$ to estimate $CMRO_2$ and CBF simultaneously from a single session of a PET scan (Kudomi et al, 2005). This protocol, however, required a separation of a RW TAC from the whole blood TAC as showed recently (Kudomi et al, 2007).

The k_{BM} determined from the total body oxygen metabolism, namely the BM approach, was significantly greater than k obtained by the 4PF or the 1PF approach, by a factor 2, as shown in Figure 4. The reason is not clear, but partly attributed to the limitation of the simplified model. The body system consists of various organs which have different oxygen metabolism along with different circulation systems and with transit times. It is well known that the apparent rate constant defined with a simplified compartmental model could be underestimated as compared with an average of true rate constants, known as heterogeneity effects (Iida et al, 1989; Aston et al, 2002). This is, however, not essential.

208

Simply, linear correction could be applied to convert to the apparent k value as has been performed in this study. CMRO$_2$ values calculated using BM approach for the RW separation, were in good agreement with those determined with the direct measurement of RW as shown in Table 3.

The current method with modeling approach and simplified procedure provided consistent results in terms of time-dependent RW component, and consequently metabolic product of $^{15}O_2$ was separated from arterial whole blood for the CMRO$_2$ assessment in PET examination. The modeling approach to separate metabolite from authentic tracer has been showed previously for 6-[^{18}F]fluoro-L-dopa study (fdopa) (Huang et al, 1991). We expect that the modeling approach in conjunction with the simplified method showed in our study could be applied for various kinds of tracers, which require the separation of metabolic product such as fdopa. This approach enables us to assess parametric images for those tracers by eliminating the laborious procedures and by avoiding the amount of blood samplings, particularly for smaller animals.

In conclusion, the present RW model was feasible to reproduce RW TAC from a whole radioactivity concentration curve obtained after $^{15}O_2$ inhalation, and for a wide range of species. The simplified procedure to predict the RW TAC is of use to calculate CMRO$_2$ in smaller animals as well as clinical patients.

Acknowledgements

References

Aston JA, Cunningham VJ, Asselin MC, Hammers A, Evans AC, Gunn RN (2002) Positron emission tomography partial volume correction: estimation and algorithms. J Cereb Blood Flow Metab 22:1019–34

Eriksson L, Holte S, Bohm Chr, Kesselberg M, Hovander B (1988) Automated blood sampling system for positron emission tomography. IEEE Trans Nucl Sci 35:703–7

Eriksson L, Kanno I (1991) Blood sampling devices and measurements. Med Prog Technol 17:249–57

Fujita H, Kuwabara H, Reutens DC, Gjedde A (1999) Oxygen consumption of cerebral cortex fails to increase during continued vibrotactile stimulation. J Cereb Blood Flow Metab 19:266–71

Hayashi T, Watabe H, Kudomi N, Kim KM, Enmi J, Hayashida K, Iida H (2003) A theoretical model of oxygen delivery and metabolism for physiologic interpretation of quantitative cerebral blood flow and

metabolic rate of oxygen. J Cereb Blood Flow Metab 23:1314–23

Hirano T, Minematsu K, Hasegawa Y, Tanaka Y, Hayashida K, Yamaguchi T (1994) Acetazolamide reactivity on ^{123}I-IMP single photon emission computed tomography in patients with major cerebral artery occlusive disease: correlation with positron emission tomography parameters. J Cereb Blood Flow Metab 14:763–70

Holden JE, Eriksson L, Roland PE, Stone-Elander S, Widen L, Kesselberg M (1988) Direct comparison of single-scan autoradiographic with multiple-scan least-squares fitting approaches to PET CMRO$_2$ estimation. J Cereb Blood Flow Metab 8:671–80

Huang SC, Barrio JR, Yu DC, Chen B, Grafton S, Melega WP, Hoffman JM, Satyamurthy N, Mazziotta JC, Phelps ME (1991) Modelling approach for separating blood time-activity curves in positron emission tomographic studies. Phys Med Biol 36:749–61

Iida H, Jones T, Miura S (1993) Modeling approach to eliminate the need to separate arterial plasma in oxygen-15 inhalation positron emission tomography. J Nucl Med 34:1333–40

Iida H, Kanno I, Miura S, Murakami M, Takahashi K, Uemura K (1989) A determination of the regional brain/blood partition coefficient of water using dynamic positron emission tomography. J Cereb Blood Flow Metab 9:874–85

Kaisti KK, Langsjo JW, Aalto S, Oikonen V, Sipila H, Teras M, Hinkka S, Metsahonkala L, Scheinin H (2003) Effects of sevoflurane, propofol, and adjunct nitrous oxide on regional cerebral blood flow, oxygen consumption, and blood volume in humans. Anesthesiology 99:603–13

Kudomi N, Choi C, Watabe H, Kim KM, Shidahara M, Ogawa M, Teramoto N, Sakamoto E, Iida H (2003) Development of a GSO detector assembly for a continuous blood sampling system. IEEE Trans Nucl Sci 50:70–3

Kudomi N, Hayashi T, Teramoto N, Watabe H, Kawachi N, Ohta Y, Kim KM, Iida H (2005) Rapid quantitative measurement of CMRO$_2$ and CBF by dual administration of ^{15}O-labeled oxygen and water during a single PET scan—a validation study and error analysis in anesthetized monkeys. J Cereb Blood Flow Metab 25:1209–24

Kudomi N, Watabe H, Hayashi T, Iida H (2007) Separation of input function for rapid measurement of quantitative CMRO$_2$ and CBF in a single PET scan with a dual tracer administration method. Phys Med Biol 52:1893–908

Laforest R, Sharp TL, Engelbach JA, Fettig NM, Herrero P, Kim J, Lewis JS, Rowland DJ, Tai YC, Welch MJ (2005) Measurement of input functions in rodents: challenges and solutions. Nucl Med Biol 32:679–85

Lindstedt L, Schaeffer PJ (2002) Use of allometry in predicting anatomical and physiological parameters of mammals. Lab Anim 36:1–19

Magata Y, Temma T, Iida H, Ogawa M, Mukai T, Iida Y, Morimoto T, Konishi J, Saji H (2003) Development of injectable O-15 oxygen and estimation of rat OEF. J Cereb Blood Flow Metab 23:671–6

Meyer E, Tyler JL, Thompson CJ, Redies C, Diksic M, Hakim AM (1987) Estimation of cerebral oxygen utilization rate by single-bolus 15O2 inhalation and dynamic positron emission tomography. J Cereb Blood Flow Metab 7:403–14

Mintun MA, Raichle ME, Martin WR, Herscovitch P (1984) Brain oxygen utilization measured with O-15 radio-

10

tracers and positron emission tomography. *J Nucl Med* 25:177–87

Mintun MA, Vlassenko AG, Shulman GL, Snyder AZ (2002) Time-related increase of oxygen utilization in continuously activated human visual cortex. *Neuroimage* 16:531–7

Ohta S, Meyer E, Thompson CJ, Gjedde A (1992) Oxygen consumption of the living human brain measured after a single inhalation of positron emitting oxygen. *J Cereb Blood Flow Metab* 12:179–92

Okazawa H, Yamauchi H, Sugimoto K, Takahashi M, Toyoda H, Kishibe Y, Shio H (2001a) Quantitative comparison of the bolus and steady-state methods for measurement of cerebral perfusion and oxygen metabolism: positron emission tomography study using 15O-gas and water. *J Cereb Blood Flow Metab* 21:793–803

Okazawa H, Yamauchi H, Sugimoto K, Toyoda H, Kishibe Y, Takahashi M (2001b) Effects of acetazolamide on cerebral blood flow, blood volume, and oxygen metabolism: a positron emission tomography study with healthy volunteers. *J Cereb Blood Flow Metab* 21:1472–9

Pain F, Laniece P, Mastrippolito R, Gervais P, Hantraye P, Besret L (2004) Arterial input function measurement without blood sampling using a beta-microprobe in rats. *J Nucl Med* 45:1577–82

Sakoh M, Gjedde A (2003) Neuroprotection in hypothermia linked to redistribution of oxygen in brain. *Am J Physiol Heart Circ Physiol* 285:H17–25

Shidahara M, Watabe H, Kim KM, Oka H, Sago M, Hayashi T, Miyake Y, Ishida Y, Hayashida K, Nakamura T, Iida H (2002) Evaluation of a commercial PET tomograph-based system for the quantitative assessment of rCBF, rOEF and rCMRO2 by using sequential administration of 15O-labeled compounds. *Ann Nucl Med* 16:317–27

Temma T, Magata Y, Kuge Y, Shimonaka S, Sano K, Katada Y, Kawashima H, Mukai T, Watabe H, Iida H, Saji H (2006) Estimation of oxygen metabolism in a rat model of permanent ischemia using positron emission tomography with injectable$^{15}O-O_2$. *J Cereb Blood Flow Metab* 26:1577–83

Vafaee MS, Gjedde A (2000) Model of blood-brain transfer of oxygen explains nonlinear flow-metabolism coupling during stimulation of visual cortex. *J Cereb Blood Flow Metab* 20:747–54

Votaw JR, Shulman SD (1998) Performance evaluation of the Pico-Count flow-through detector for use in cerebral blood flow PET studies. *J Nucl Med* 39:509–15

Weber B, Burger C, Biro P, Buck A (2002) A femoral arteriovenous shunt facilitates arterial whole blood sampling in animals. *Eur J Nucl Med Mol Imaging* 29: 319–23

Wessen A, Widman M, Andersson J, Hartvig P, Valind S, Hetta J, Langstrom B (1997) A positron emission tomography study of cerebral blood flow and oxygen metabolism in healthy male volunteers anaesthetized with eltanolone. *Acta Anaesthesiol Scand* 41:1204–12

Yamauchi H, Okazawa H, Kishibe Y, Sugimoto K, Takahashi M (2003) The effect of acetazolamide on the changes of cerebral blood flow and oxygen metabolism during visual stimulation. *Neuroimage* 20:543–9

Yee SH, Lee K, Jerabek PA, Fox PT (2006) Quantitative measurement of oxygen metabolic rate in the rat brain using microPET imaging of briefly inhaled 15O-labelled oxygen gas. *Nucl Med Commun* 27:573–81

Optimal scan time of oxygen-15-labeled gas inhalation autoradiographic method for measurement of cerebral oxygen extraction fraction and cerebral oxygen metabolic rate

Miho Shidahara · Hiroshi Watabe · Kyeong Min Kim
Nobuyuki Kudomi · Hiroshi Ito · Hidehiro Iida

Abstract

Objective Regional cerebral blood flow (CBF), cerebral blood volume, oxygen extraction fraction (OEF), and cerebral metabolic rate of oxygen (CMRO$_2$) can be estimated from C^{15}O, H$_2^{15}$O, and ^{15}O$_2$ tracers and positron emission tomography (PET) using an autoradiographic (ARG) method. Our objective in this study was to optimize the scan time for ^{15}O$_2$ gas study for accurate estimation of OEF and CMRO$_2$.

Methods We evaluated statistical noise in OEF by varying the scan time and error caused by the tissue heterogeneity in estimated OEF and CMRO$_2$ using computer simulations. The characteristics of statistical noise were investigated by signal-to-noise (S/N) ratio from repeated tissue time activity curves with noise, which were generated using measured averaged arterial input function and assuming CBF = 20, 50, and 80 (ml/100 g per minute). Error caused by tissue heterogeneity was also investigated by estimated OEF and CMRO$_2$ from tissue time activity curve with mixture of gray and white matter varying fraction of mixture. In the simulations, three conditions were assumed (i) CBF in gray and white matter (CBF^g and CBF^w) was 80 and 20, OEF in gray and white matter (E^g and E^w) was 0.4 and 0.3, (ii) CBF^g and CBF^w decreased by 50%, and E^g and E^w increased by 50% when compared with conditions (i) and (iii). CBF^g and CBF^w decreased by 80%, and E^g and E^w increased by 50% when compared with condition (i).

Results The longer scan time produced the better S/N ratio of estimated OEF value from three CBF values (20, 50, and 80). Errors of estimated OEF for three conditions owing to tissue heterogeneity decreased, as scan time took longer. Meanwhile in the case of CMRO$_2$, 3 min of scan time was desirable.

Conclusions The optimal scan time of ^{15}O$_2$ inhalation study with the ARG method was concluded to be 3 min from taking into account for maintaining the S/N ratio and the quantification of accurate OEF and CMRO$_2$.

Introduction

Quantitative cerebral oxygen extraction fraction (OEF) and cerebral metabolic rate of oxygen (CMRO$_2$) images can be measured by oxygen-15-labeled gas (^{15}O$_2$) and positron emission tomography (PET). These physiological parameters have provided important hemodynamic information for the diagnoses of cerebrovascular disease, especially in the case of misery perfusion [1–3]. For effective application of these parameters to urgent clinical study, a simplified diagnostic method to shorten scan time is strongly required and yet retaining the quantification. When compared with the steady-state method, the autoradiographic (ARG) method [4] has the potential to shorten the length of study [5]. A 3-min scan duration following ^{15}O$_2$ inhalation has been used by Hatazawa et al. [6]; however, earlier no systematic investigation of optimization of scan time for ^{15}O$_2$ study with the ARG method was performed. In this article, by focusing on two factors, namely, signal-to-noise (S/N) ratio on the

M. Shidahara (✉) · H. Ito
Molecular Imaging Center, National Institute of Radiological Sciences, 4-9-1 Anagawa, Inage-ku, Chiba 263-8555, Japan
e-mail: sidahara@nirs.go.jp

H. Watabe · K.M. Kim · N. Kudomi · H. Iida
Department of Investigative Radiology, National Cardiovascular Center Research Institute, Osaka, Japan

functional images and the tissue heterogeneity, the optimal scan duration for the ARG method with $^{15}O_2$ gas was investigated.

Variance of pixel counts in reconstructed image is delivered from randomly emitted and detected photon counts and then propagates to estimated OEF and $CMRO_2$ value. The short physical half-life (about 2 min) of ^{15}O causes large variance of the pixel counts, and, therefore, alternation of the scan duration leads to substantial change on the image quality of PET image, such as S/N ratio.

The influence of tissue heterogeneity on estimated physiological parameters has been reported by several authors [7, 8], and estimation error of cerebral blood flow (CBF) is caused by the assumption that there is only single-tissue CBF in mixed region of gray and white matter, even though different tissues own different CBF values. An optimization scheme of measurement of CBF was provided by Kanno et al. [7, 9], and that study showed the error of estimated CBF from tissue heterogeneity depended on scan time [9]. The effect of tissue heterogeneity in systematic error of OEF has been also analyzed for the steady-state method [10, 11]. However, in the case of the estimation of OEF and $CMRO_2$ with the ARG method and bolus inhalation of $^{15}O_2$, the effects of tissue heterogeneity in $^{15}O_2$ study and the effect of the error in CBF owing to tissue heterogeneity propagates to OEF and $CMRO_2$ estimates are unknown.

In this article, we performed computer simulations of the ARG method with ^{15}O water and $^{15}O_2$ gas under three clinical conditions, namely, normal, misery perfusion, and occlusion. We investigated the relationship between scan time and S/N ratio of estimated OEF. Furthermore, the relationship between scan time and the accuracy in estimated OEF and $CMRO_2$ affected by tissue heterogeneity for both ^{15}O water and $^{15}O_2$ gas studies was examined. By these results, optimized scan time for $^{15}O_2$ gas inhalation protocol was determined especially for clinical application such as ischemic disease.

Materials and methods

Computing CBF, OEF, and $CMRO_2$ using the ARG method

In the ARG method, CBF (ml/g per minute) is computed by a single-tissue compartment model described as follows:

$$\int_0^T C_t^W(t)\mathrm{d}t = \rho_b \int_0^T CBF \cdot A(t) \otimes e^{-\rho_b \frac{CBF}{p}} \, \mathrm{d}t \qquad (1)$$

where $C_t^W(t)$ (cps/ml) is the radioactivity concentration of $H_2^{15}O$ study at time t measured by PET (integrated from time 0 to time T), ρ_b is the density of brain tissue (1.04) (g/ml), $A(t)$ (cps/ml) is arterial input function of $H_2^{15}O$ at time t measured by the external radiation detector, and p is the partition coefficient factor (fixed as 0.8 ml/ml) [12]. The CBF value for each pixel is estimated in the look-up table manner with observer PET data $\int_0^T C_t^W(t)\mathrm{d}t$ against $\rho_b \int_0^T CBF \cdot A(t) \otimes e^{-\rho_b \frac{CBF}{p}} \, \mathrm{d}t$.

Using the ARG method, OEF and $CMRO_2$ are computed owing to a model by Mintun et al. [4] described as follows:

$$\int_0^T C_t^O(t)\mathrm{d}t = \rho_b \int_0^T CBF \cdot A_{H_2O}(t) \otimes e^{-\rho_b \frac{CBF}{p}}$$
$$+ OEF \cdot CBF \cdot A_{O_2}(t) \otimes e^{-\rho_b \frac{CBF}{p}t}$$
$$+ CBV \cdot VR \cdot (1 - OEF \cdot FV) \cdot A_{O_2}(t)\mathrm{d}t \qquad (2)$$

where $C_t^O(t)$ (cps/ml) is the radioactivity concentration of $^{15}O_2$ study at time t measured by PET (integrated from time 0 to time T), CBF (ml/g per minute) values are obtained from $H_2^{15}O$ study using Eq. 1, $A_{H_2O}(t)$ (cps/ml) and $A_{O_2}(t)$ (cps/ml) are the arterial input functions for $H_2^{15}O$ and $^{15}O_2$ components at time t measured by the external radiation detector. CBV is the cerebral blood volume and calculated by the additional PET scan with $C^{15}O$. VR is the small- to large-vessel hematocrit ratio (fixed as 0.85), FV is the effective venous fraction (fixed as 0.835) [4]. OEF is computed from the arterial input functions of $A_{H_2O}(t)$ and $A_{O_2}(t)$ and fixed values for p, VR and FV by the look-up table manner in the pixel-by-pixel basis. $CMRO_2$ is then calculated as follows:

$$CMRO_2 = CBF \cdot OEF \cdot [O_2]_a \qquad (3)$$

where $[O_2]_a$ is the arterial oxygen concentration which is given as follows:

$$[O_2]_a = 1.39 \cdot Hb \cdot \%Sat \qquad (4)$$

where 1.39 is the averaged oxygen volume associated with a single hemoglobin molecule, Hb is the hemoglobin concentration (g hemoglobin/ml blood), and %Sat is the percentage of saturation in O_2 of the arterial blood.

PET study

To compute CBF, OEF, and $CMRO_2$ images, three PET scans with $C^{15}O$ gas, ^{15}O water, and $^{15}O_2$ gas are required with additional transmission scan. The typical clinical

protocol in National Cardiovascular Center Hospital is as follows:

1. Ten-minute transmission scan with ^{68}Ge–^{68}Ga source.
2. The subject was made to inhale C^{15}O (2.19 MBq per minute) for 1 min and 4 min after the start of the inhalation; PET scan is started for 4 min.
3. The subject is intravenously (right bronchial vein) administered H$_2$^{15}O (0.81 MBq for 20 s bolus injection). PET scan (12 × 5 s, 2 × 15 s total 1.5 min) is started 10 s later from the start of infusion of H$_2$^{15}O.
4. The subject was made to inhale ^{15}O$_2$ gas (2.19 MBq/min) for 1 min. PET scan (12 × 5 s, 8 × 15 s total 3 min) is started at the same time of the inhalation.

Positron emission tomography scanner is ECAT EXACT 47 (CTI, Knoxville, TN, USA), and all scans are performed with 2D mode (septa extended). For the present study, scan protocol of ^{15}O$_2$ gas was extended from conventional 180 s to 300 s (12 × 5 s, 8 × 15 s, and 4 × 30 s).

For the simulations studies, arterial input functions of $A_{H_2O}(t)$ and $A_{O_2}(t)$ in Eq. 2 were mimicked from averaged whole-blood arterial input function of five healthy volunteers (all subjects were men, and mean age was 24.7 ± 3.6 years) [13]. Delay- and dispersion-corrected arterial input functions of the five subjects were averaged and separated into two-component, oxygen-gas, and metabolized water by convolution formula [14] (Fig. 1).

Simulation studies

Two simulation studies were performed.

Simulation 1: S/N ratio in quantitative OEF images

The relationship between the scan duration and statistical noise of OEF values was investigated in terms of S/N ratio. The variance of PET data C_{PET} at frame i was estimated using the following equation [15, 16]:

$$\frac{\sigma(i)}{C_{PET}(i)} = \frac{c}{\sqrt{NEC(i)}} \tag{5}$$

where $\sigma(i)$ is standard deviation (SD) of C_{PET} at frame i and NEC(i) is noise equivalent count [17] at frame i. c is constant factor. To determine c, phantom experiments were performed. A cylindrical phantom (16 cm in diameter and an axial length of 20 cm) filled with water was used for the measurement of statistical noise on reconstructed image. ^{15}O water solution (half-life is 2.04 min, 518 MBq at scan start) was injected in the phantom.
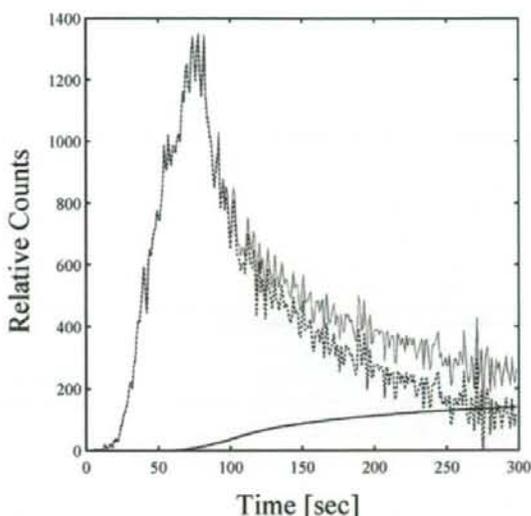

Fig. 1 Delay- and dispersion-corrected arterial input function: whole-blood curve [function: whole-blood curve (*solid line*), O$_2$ components (*dotted line*), and metabolized water components (*bold solid line*)]

Single-PET scanning with dynamic acquisition was performed to obtain 20 frames, each with duration of 60 s. Count rates of true coincidents and random coincidents detected by PET gantry were also recorded, and NEC for each frame was computed. Image reconstruction was performed by direct Fourier transform algorithm with 6.0 mm full width half maximum Gaussian filter that is used for the clinical routine. From each frame data, mean $C_{PET}(i)$ with $\sigma(i)$ were computed from all pixels inside the drawn circular ROI (10 cm in diameter) on the reconstructed image. The constant c was estimated by these data to fit Eq. 5.

To simulate the S/N ratio in the clinical PET study, NEC(i) during PET acquisition was measured in actual PET studies with ^{15}O$_2$ gas for five normal volunteers described in earlier section and the averaged NEC(i) data were used in the simulation; 500 noisy simulated PET data, $C'_{PET}(i)$ ($j = 1, \ldots, 500$) were generated according to Eqs. 2 and 5 under the conditions of CBF = 20, 50, and 80 (ml/100 g per minute) and OEF = 0.2, 0.4, and 0.8. The integration time T in Eq. 2 was set to 60 s, 120 s, 180 s, 240 s, and 300 s and at each integration time T, OEF^j(T) was estimated from each $\int_0^T C_{PET}^j(i)di$ using the ARG method. The S/N ratios at time T were derived from the division of mean estimated OEF(T) using 500 data sets by its SD.

$\underline{\textcircled{\tiny 2}}$ Springer

Table 1 Predefined parameters for simulations of tissue heterogeneity

Condition	CBF^g (ml/100 g per minute)	CBF^w (ml/100 g per minute)	OEF^g	OEF^w
(i) Normal	80	20	0.4	0.3
(ii) Misery perfusion	40	10	0.6	0.45
(iii) Occlusion	16	4	0.6	0.45

Three conditions of (i) normal, (ii) misery perfusion, and (iii) occlusion were considered. Cerebral blood flow (CBF) in gray matter (CBF^g) and white matter (CBF^w), and oxygen extraction fraction (OEF) in gray matter (OEF^g) and white matter (OEF^w) were defined

Simulation 2: Tissue heterogeneity

The time dependency of quantitative error in estimated OEF and CMRO$_2$ caused by tissue heterogeneity was evaluated. We assumed that tissue TAC $C_i^m(t)$ in a mixed region of gray and white matter is expressed as

$$C_i^m(t) = \alpha \cdot C_i^g(t) + (1 - \alpha) \cdot C_i^w(t) \tag{6}$$

where α is the fraction of gray matter volume ranged from 0 to 1, and $C_i^g(t)$ and $C_i^w(t)$ are calculated tissue TACs in gray and white matter from Eqs. 1 and 2 with fixed parameters, respectively. In view of the clinical application for ischemic disease, three physiological conditions of (i) normal, (ii) misery perfusion, and (iii) occlusion were considered in the present simulations. CBF in gray matter and white matter, and OEF in gray matter and white matter were defined as shown in Table 1. CBF^m, OEF^m, and CMRO$_2^m$, including the effect of tissue heterogeneity was estimated by the ARG method with the integration time T of 90 s in H$_2^{15}$O study and $T = 120$ s, 180 s, 240 s, and 300 s in ^{15}O$_2$ study.

The magnitude of error in estimated CBF^m value at fixed scanning time of 90 s

Varying the fraction of gray volume [0 : 1], CBF^m of three conditions in (i), (ii), and (iii) was estimated by the ARG method and the differences between CBF^m and ideal CBF value CBF$_{ave}$ in Eq. 7 were compared.

$$CBF_{ave} = \alpha \cdot CBF_g + (1 - \alpha) \cdot CBF_w \tag{7}$$

Time dependency of estimated OEF^m from CBF^m

For three conditions, OEF$^m(T)$ and CMRO$_2^m(T)$ at integration time T (= 120 s, 180 s, 240 s, and 300 s) were estimated using CBF^m value and the ARG method. Varying the fraction of gray volume [0:1] for H$_2^{15}$O and ^{15}O$_2$ study, OEF^m and CMRO$_2^m$ were compared with ideal OEF and CMRO$_2$ values (OEF$_{ave}$ and CMRO$_{2ave}$), shown in Eq. 8:

$$OEF_{ave} = \alpha \cdot OEF^g + (1 - \alpha) \cdot OEF^w$$
$$CMRO_{2ave} = \alpha \cdot CMRO_2^g + (1 - \alpha) \cdot CMRO_2^w \tag{8}$$

In the calculations of CMRO$_2^m$, CBF^m values were employed.

Results

Simulation 1: S/N ratio in quantitative OEF images

Figure 2a shows the relationship between NEC and coefficient of variance (COV) which is defined as the ratio between SD of C_{PET} and C_{PET}. Constant factor c in Eq. 5 was estimated from the relationship using the least-squares fitting and resulted in 38.1 ($r = 0.996$). Figure 2b shows averaged NEC curve of 5 ^{15}O$_2$ studies.

Oxygen extraction fraction under the condition of CBF = 20, 50, and 80 (ml/100 g per minute) was estimated using noise-added time activity curve (Fig. 3a) using calculated $\sigma(i)$ in Eq. 5 and averaged NEC curve. Figure 3 shows the relationship between integrated time T and S/N ratio in estimated OEF values [OEF = 0.4 (Fig. 3b), OEF = 0.2 (Fig. 3c), and OEF = 0.6 (Fig. 3d)]. In general, the longer scan time provided better S/N ratio as shown in Fig. 3. In the case of low OEF (i.e., OEF = 0.2), S/N ratio reached plateau more rapidly than other cases.

Actual OEF and CMRO$_2$ images computed by the ARG method with $T = 60$ s, 180 s for a young normal volunteer were shown in Fig. 4. Less statistical noise in both OEF and CMRO$_2$ images with $T = 180$ s was visually observed when compared with $T = 60$ s. This figure supports the simulation results.

Simulation 2: Tissue heterogeneity

The relationship between the error of estimated CBF^m for H$_2^{15}$O study and the fraction of gray volume is shown in Fig. 5. Lower CBF values in both gray and white matters [i.e., condition (ii) CBF^g = 40, CBF^w = 10, or condition (iii) CBF^g = 16, CBF^w = 4] reduce the error of

Fig. 2 a The relationship
between noise equivalent
count (NEC) and coefficient
of variance (COV) obtained
from phantom experiment
with ECAT EXACT. b
Averaged dynamic NEC
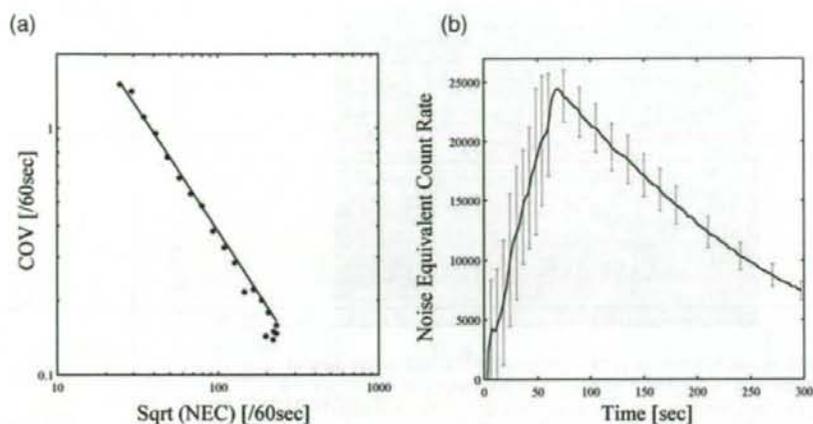curve with standard deviation
of $^{15}O_2$ study among five
volunteers

Fig. 3 a Noise-added time
activity curves of $^{15}O_2$ study
assuming oxygen extraction
fraction (OEF) = 0.4 and
cerebral blood flow (CBF) =
80 (open circle), 50 (closed
circle), and 20 (cross; ml/100 g
per minute), and true time
activity curves (dotted lines).
Time dependency of signal-to-
noise ratio in estimated (b)
OEF = 0.4, (c) OEF = 0.2,
and (d) OEF = 0.6 using CBF
= 80 (open circle), 50 (closed
circle), and 20 (cross; ml/100 g
per minute)
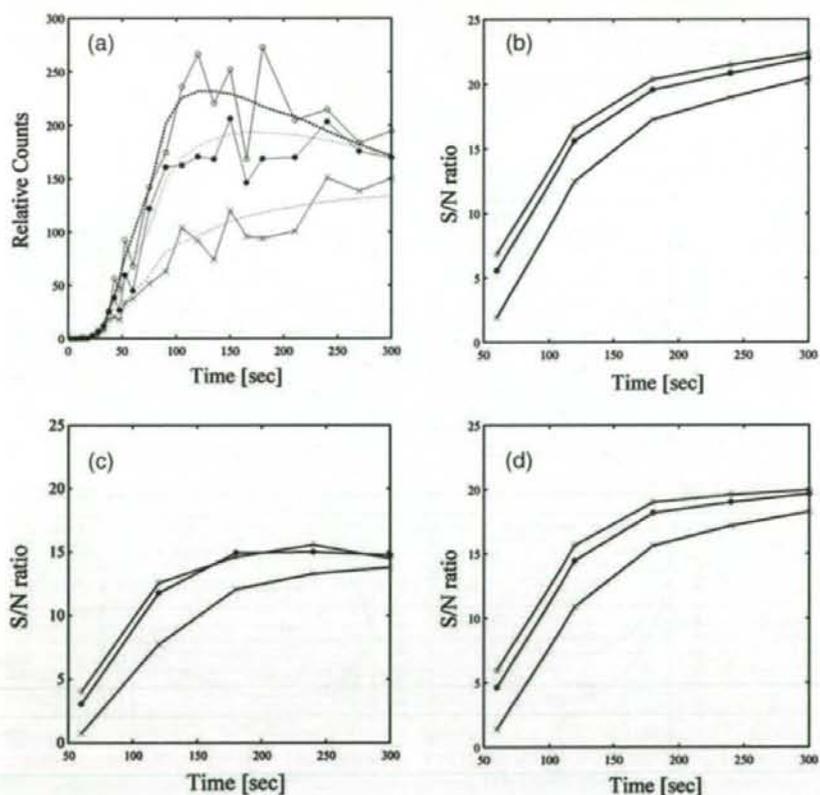
estimated CBF^m when compared with condition (i)
$CBF^g = 80$, $CBF^w = 20$. The maximum error of CBF^m
with three conditions of (i) normal, (ii) misery perfusion,
and (iii) occlusion were −12.5% ($\alpha = 0.39$), −6.7%
($\alpha = 0.38$), and −2.8% ($\alpha = 0.35$), respectively.

Figures 6 and 7 show the relationship between the
error of estimated $OEF^m(T)$ (a) and $CMRO_2^m(T)$ (b)
and the relationship between the maximum error and
scanning time. As shown in Fig. 7a, b, by increasing
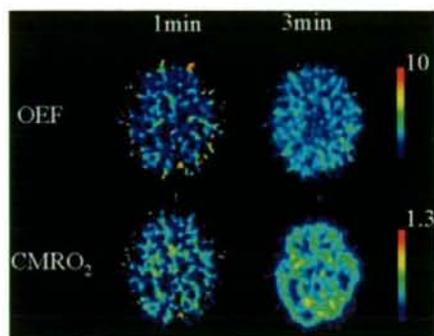integration time, the error of estimated OEF^m and

Fig. 4 An example of clinical images of OEF and cerebral metabolic rate of oxygen (CMRO$_2$) obtained from $T = 60$ s and 180 s scan time for a patient. Image reconstruction was performed with direct Fourier transform algorithm with 6 mm Gaussian filter. Reconstructed image has $128 \times 128 \times 47$ slices with 1.84 mm $\times$ 1.84 mm and 3.38 mm pixel sizes. Attenuation correction using transmission data and scatter correction with the deconvolution scatter function were applied
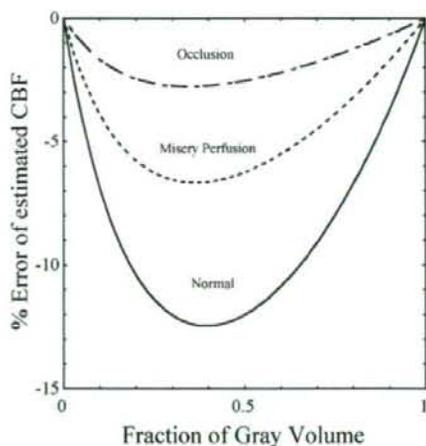

Fig. 5 The effect of tissue heterogeneity on % error of CBF^m in CBF^g = 80, CBF^w = 20 (*solid line*), CBF^g = 50, CBF^w = 12 (*dotted line*), and CBF^g = 16, CBF^w = 4 (*dotted dashed line*)
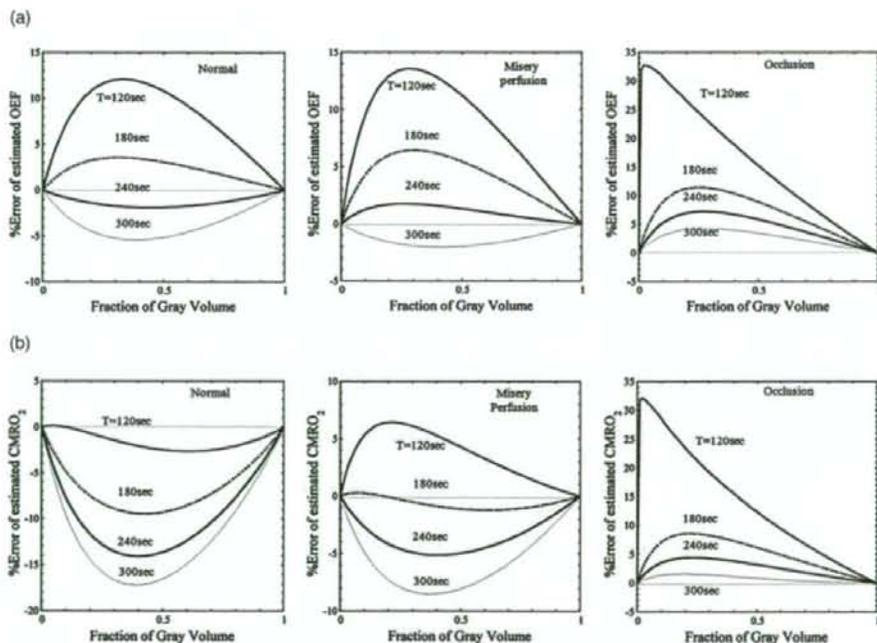

Fig. 6 The effect of tissue heterogeneity on % error of OEF^m (*T*) (**a**) and CMRO$_2$^{m} (*T*) (**b**) in normal, misery perfusion, and occlusion conditions for integration times of 120 s, 180 s, 240 s, and 300 s including the effect of tissue heterogeneity in H$_2$^{15}O study

Fig. 7 The maximum error of estimated OEF^m (T) (a) and $CMRO_2^m$ (T) (b) for integration times of 120 s, 180 s, 240 s, and 300 s including the effect of tissue heterogeneity in $H_2^{15}O$ study. *Solid lines* are for normal conditions. *Dotted lines* are for misery perfusion conditions. *Dotted dashed lines* are for occlusion conditions
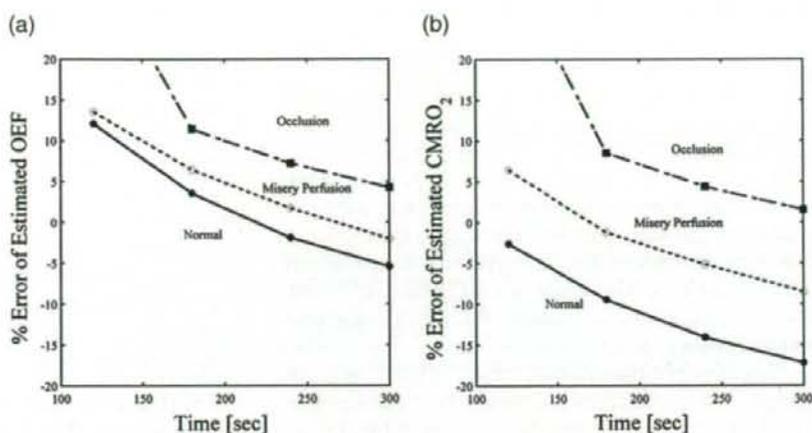
$CMRO_2^m$ tended to become negative values. In detail, for occlusion condition (iii) longer integration time provided smaller error of estimated OEF^m and $CMRO_2^m$. In misery perfusion condition (ii), the error of estimated OEF^m also became smaller error until 300 s, and then the error tended to become negative. The error of estimated $CMRO_2^m$ for condition (ii) is minimized to −1.22% at 180 s accumulation time. In normal condition (i), the error of estimated OEF^m was minimized to −1.9% at 240 s, and the error of estimated $CMRO_2^m$ was minimized to −2.63% at 120 s.

Discussion

In this study, for proper scan protocol of the ARG method in ^{15}O, study, we simulated time dependency of accuracy and variation in physiological parameters with statistical noise and effect of tissue heterogeneity.

S/N ratio in estimated OEF

Variance of pixel counts in reconstructed images is delivered from randomly emitted and detected photon counts and then propagates to estimated OEF and $CMRO_2$ values. Actually, the statistical model of variance of pixel counts does not simply obey the Poisson statistics owing to several data processing (normalization, attenuation, and scatter corrections), which destroy the statistical relationship between expected and observed values. Earlier, there were investigations on developing the statistical model of pixel value [7, 15, 16]. Carson et al. [15] and Watabe et al. [16] modeled statistical variation of pixel value using NEC and then evaluated the adaptability of the model by the phantom and clinical studies.

Their approach is simple and accurate enough, and so, we utilized their approach to simulate the noise.

We simulated the TAC $C_i(t)$ from lower to higher count level using three cases of CBF = 20, 50, and 80 (ml/100 g per minute) under three conditions of OEF values (0.2, 0.4, and 0.6), because the variation in OEF depends on the TAC counts level. As shown in Fig. 3, the longer scan time provides better S/N ratio. This figure indicates that the S/N ratio with low OEF and high CBF (Fig. 3c) reaches a plateau earlier than other cases. This is because that later points of TAC with low OEF and high CBF have little impact on the noise of estimates. Because $CMRO_2$ is the product with OEF and CBF, the characteristic of statistical noise of estimated $CMRO_2$ could be propagated from estimated OEF as well as estimated CBF values. Therefore, the maximum S/N ratio of the estimated $CMRO_2$ expects to show the same tendency as the S/N ratio of the estimated OEF if the statistical noise of the CBF was fixed.

In the present study, we assumed the noise-free arterial input function for the simulation. Furthermore, we added noise to arterial input function, but the tendency did not change (data are not shown).

Tissue heterogeneity

We showed that in the mixed region of gray and white matter, the non-linear relationship between physiological parameters and PET counts results in over-/underestimation of the physiological parameters. Figure 5 shows that a lower CBF such as ischemic disease leads to a small error of estimated CBF^m when compared with normal CBF because that effect of the non-linear relationship is less dominant than in the case of a high CBF value. This is consistent with results that Ito et al. [8]

showed high CBF value is more suffered from the tissue heterogeneity when compared with that low CBF value in SPECT study [8]. For the ARG PET study with $H_2^{15}O$ study, earlier research by Kanno et al. showed about 13% underestimation in estimated CBF owing to tissue heterogeneity for scan time, 120 s, assuming $CBF^g = 80$, $CBF^w = 20$, $P = 1.0$, and gray matter fraction = 0.5 [9]. Even though there were slight differences in partition coefficient and scan time between Kanno et al. [9] and our study, underestimation in estimated CBF was about 12% for scan time 90 s, assuming $CBF^g = 80$, $CBF^w = 20$, $P = 0.9$, and gray matter fraction = 0.5, which was almost similar results to Kanno et al. [9].

The errors of estimated OEF^m and $CMRO_2^m$ are propagated from such error of estimated CBF^m. As shown in Fig. 7, the results of the present study suggest that error of estimated physiological parameters with tissue heterogeneity will variously change positive or negative under the conditions (i), (ii), and (iii) with various scan times. The shorter scan time, the more overestimation was observed for OEF^m under the conditions (i), (ii), and (iii), and $CMRO_2^m$ especially under the condition (iii). This may be caused from the underestimation of CBF^m, which can be assumed to be the lower oxygen-15 oxy-hemoglobin supplement than true oxygen-15 oxy-hemoglobin supplement (= observed or simulated PET counts) especially at the early scan time, when the metabolized water component can be neglected. In the longer scan time, the more underestimation was observed for OEF^m under the conditions (i) and (ii) and $CMRO_2^m$ especially under the condition (i). There are earlier studies on tissue heterogeneity in estimated OEF for the steady-state method [10, 11]. Without considering error in estimated CBF, Lammertsma and Jones [10] showed that OEF values for every condition were underestimated owing to tissue heterogeneity. Correia et al. [11] investigated the effect of tissue heterogeneity on OEF considering the error in estimated CBF under the condition of the steady state. According to their studies, a small OEF^g value (i.e., $OEF^g = 0.2$, $OEF^w = 0.4$) leads to overestimation in OEF, and a large OEF^g value ($OEF^g = 0.8$, $OEF^w = 0.4$) leads to underestimation in OEF. Interestingly, the overestimation in estimated large OEF^g (i.e., $OEF^g = 0.6$, $OEF^w = 0.45$ especially in occlusion case) in our study was different from the underestimation in estimated large OEF^g by Correia et al. and this may be caused by different methodologies used (steady-state or autoradiography).

To optimize the scan time for the $^{15}O_2$ scan, it is important to consider not only the error in OEF^m and $CMRO_2^m$ but also the error in CBF^m derived from the ^{15}O water scan, which is unavoidable factor. Considering the variation of OEF and $CMRO_2$, tissue heterogeneity, and applicability for clinical study, the optimal scan

time of 3 min is suggested owing to following three reasons:

1. At the point of S/N of OEF and $CMRO_2$, the longer scan time is adequate (Fig. 3).
2. In terms of estimating OEF under circumstance of tissue heterogeneity, the longer scan time is adequate (Fig. 7a).
3. As shown in Fig. 7b, longer scan time has been required for $CMRO_2^m$ under the condition (iii). Conversely, shorter scan time has been required for $CMRO_2^m$ under the condition (i). The minimum error of $CMRO_2^m$ under the condition (ii) was achieved at the 180 s scan time.

Alpert et al. [18] earlier commented that factors of optimal scan time for oxygen-15-labeled water study are grouped as (1) the total observation time period, (2) scan and blood sampling protocol, and (3) the type and magnitude of tracer administration. This grouping can also be applied to oxygen-15 gas study, but most facilities have already installed the equipments, and it is not so easy to change the blood sampling protocol and supplement of tracer. In this study, we discussed the optimal scan time under the conditions of fixed administration dose, inhalation time, and blood sampling protocols. It must be noted that if administration protocol is changed from 1-min inhalation without breath control to others, present optimization of scan time may not be suited.

Recently, a rapid protocol with a single-PET scan with dual-tracer ($^{15}O_2$ and $H_2^{15}O$) administration method was developed [19, 20]. They employed integrated PET data for 90 s in H_2O phase and 180 s in O_2 phase. Our strategies to optimize the scan duration could be applied for this rapid protocol to estimate CBF, OEF, and $CMRO_2$ accurately.

Kobayashi et al. [21] examined relationship between count-based OEF and scan duration. They used quantitative OEF as a standard to evaluate optimal scan duration. Although their approach to obtain OEF is different from ours, as shown in this article, the tissue heterogeneity could be another important attribution for determining the optimal scan duration.

Conclusions

In this study, we performed computer simulation studies of $^{15}O_2$ gas inhalation protocol with the ARG method. Tissue heterogeneity largely affects the quantification of estimated OEF and $CMRO_2$, and is a dominant factor in the optimization of scan time in oxygen-15 gas study. According to these simulated results, the optimal scan time for $^{15}O_2$ gas inhalation protocol is suggested to be 3 min for ischemic disease.

References

1. Ter-Pogossian MM, Herscovitch P. Radioactive oxygen-15 in the study of cerebral blood flow, blood volume, and oxygen metabolism. Semin Nucl Med 1985;15:377–94.
2. Baron JC, Bousser MG, Rey A, Guillard A, Comar D, Castaigne P. Reversal of focal "misery-perfusion syndrome" by extra-intracranial arterial bypass in hemodynamic cerebral ischemia: a case study with 15O positron emission tomography. Stroke 1981;12:454–9.
3. Gibbs JM, Wise RJ, Leenders KL, Jones T. Evaluation of cerebral perfusion reserve in patients with carotid-artery occlusion. Lancet 1984;11:310–4.
4. Mintun MA, Raichle ME, Martin WR, Herscovitch P. Brain oxygen utilization measured with O-15 radiotracers and positron emission tomography. J Nucl Med 1984;25:177–87.
5. Jones SC, Greenberg JH, Reivich M. Error analysis for the determination of cerebral blood flow with the continuous inhalation of 15O-labeled carbon dioxide and positoron emission tomograph. J Comput Assist Tomogr 1982;6:116–24.
6. Hatazawa J, Fujita H, Kanno I, Satoh T, Iida H, Miura S. Regional cerebral blood flow, blood volume, oxygen extraction fraction and oxygen utilization rate in normal volunteers measured by the autoradiographic and the single inhalation method. Ann Nucl Med 1995;9:15–21.
7. Kanno I, Iida H, Miura S, Murakami M. Optimal scan time of oxygen-15-labeled water injection method for measurement of cerebral blood flow. J Nucl Med 1991;32:1931–4.
8. Ito H, Shidahara M, Inoue K, Goto R, Kinomura S, Taki Y, et al. Effects of tissue heterogeneity on cerebral vascular response to acetazolamide stress measured by an I-123-IMP autoradiographic method with single-photon emission computed tomography. Ann Nucl Med 2005;19:251–60.
9. Kanno I, Iida H, Miura S, Murakami M, Takahashi K, Sasaki H, et al. A system for cerebral blood flow measurement using an $H_2^{15}O$ autoradiographic method and positron emission tomography. J Cereb Blood Flow Metab 1987;7:143–53.
10. Lammertsma AA, Jones T. Low oxygen extraction fraction in tumours measured with the oxygen-15 steady state technique: effect of tissue heterogeneity. Br J Radiol 1992;65:697–700.
11. Correia JA, Aplert NM, Buxton RB, Ackerman RH. Analysis of some errors in the measurement of oxygen extraction and oxygen consumption by the equilibrium inhalation method. J Cereb Blood Flow Metab 1985;5:591–9.
12. Iida H, Kanno I, Miura S, Murakami M, Takahashi K, Uemura K. A determination of the regional brain/blood partition coefficient of water using dynamic positron emission tomography. J Cereb Blood Flow Metab 1989;9:874–85.
13. Shidahara M, Watabe H, Kim KM, Oka H, Sago M, Hayashi T, et al. Evaluation of a commercial PET tomograph-based system for the quantitative assessment of rCBF, rOEF and $rCMRO_2$ by using sequential administration of ^{15}O-labeled compounds. Ann Nucl Med 2002;16:217–28.
14. Iida H, Jones T, Miura S. Modeling approach to eliminate the need to separate arterial plasma in oxygen-15 inhalation positron emission tomography. J Nucl Med 1993;34:1333–40.
15. Carson RE, Yan Y, Daube-Witherspoon ME, Freedman N, Bacharach SL, Herscovitch P. An approximation formula for the variance of PET region of interest values. IEEE Med Imaging 1993;12:240–50.
16. Watabe H, Endres CJ, Breier A, Schmall B, Eckelman WC, Carson RE. Measurement of dopamine release with continuous infusion of [11C]raclopride: optimization and signal-to-noise considerations. J Nucl Med 2000;41:522–30.
17. Strother SC, Casey ME, Hoffman EJ. Measuring PET scanner sensitivity: relating count rates to image signal-to-noise ratios using noise equivalent counts. IEEE Trans Nucl Sci 1990;37:783–8.
18. Alpert N. Optimization of regional cerebral blood flow measurements with PET (comment on J Nucl Med 1991;32:1931–4). J Nucl Med 1991;32:1934–6.
19. Kudomi N, Hayashi T, Teramoto N, Watabe H, Kawachi N, Ohta Y, et al. Rapid quantitative measurement of $CMRO_2$ and CBF by dual administration of ^{15}O-labeled oxygen and water during a single PET scan-a validation study and error analysis in anesthetized monkeys. J Cereb Blood Flow Metab 2005;25:1209–24.
20. Kudomi N, Watabe H, Hayashi T, Iida H. Separation of input function for rapid measurement of quantitative $CMRO_2$ and CBF in a single PET scan with a dual tracer. Phys Med Biol 2007;52:1893–908.
21. Kobayashi M, Kudo T, Tsujikawa T, Isozaki M, Arai Y, Fujibayashi Y, et al. Shorter examination method for the diagnosis of misery perfusion with count-based oxygen extraction fraction elevation in ^{15}O-Gas PET. J Nucl Med 2008;49:242–6.

Three-dimensional SPECT reconstruction with transmission-dependent scatter correction

Antti Sohlberg · Hiroshi Watabe · Hidehiro Iida

Abstract

Objective The quality of single-photon emission computed tomography (SPECT) imaging is hampered by attenuation, collimator blurring, and scatter. Correction for all of these three factors is required for accurate reconstruction, but unfortunately, reconstruction-based compensation often leads to clinically unacceptable long reconstruction times. Especially, efficient scatter correction has proved to be difficult to achieve. The objective of this article was to extend the well-known transmission-dependent convolution subtraction (TDCS) scatter-correction approach into a rapid reconstruction-based scatter-compensation method and to include it into a fast 3D reconstruction algorithm with attenuation and collimator-blurring corrections.

Methods Ordered subsets expectation maximization algorithm with attenuation, collimator blurring, and accelerated transmission-dependent scatter compensation were implemented. The new reconstruction method was compared with TDCS-based scatter correction and with one other transmission-dependent scatter-correction method using Monte Carlo simulated projection data of ^{99m}Tc-ECD and ^{123}I-FP-CIT brain studies.

Results The new reconstruction-based scatter compensation outperformed the other two scatter-correction methods in terms of quantitative accuracy and contrast measured with normalized mean-squared error, gray-to-white matter and striatum-to-background ratios, and also in visual quality. Highest accuracy was achieved when all the corrections (i.e., attenuation, collimator blurring, and scatter) were applied.

A. Sohlberg · H. Watabe · H. Iida (✉)
National Cardiovascular Center Research Institute,
5-7-1 Fujishiro-dai, Suita, Osaka 565-8565, Japan
e-mail: iida@ri.ncvc.go.jp

Conclusions The developed 3D reconstruction algorithm with transmission-dependent scatter compensation is a promising alternative to accurate and efficient SPECT reconstruction.

Keywords Statistical reconstruction · Scatter correction · Collimator-blurring correction · Attenuation correction

Introduction

The qualitative and quantitative accuracy of single-photon emission computed tomography (SPECT) is hampered by attenuation, collimator blurring, and scatter. Whereas attenuation and collimator blurring can nowadays be corrected in clinically acceptable times, accurate and efficient scatter correction has been proved to be a more difficult problem even though scatter compensation has received a lot of attention over the past two decades.

Scatter-correction methods can generally be divided into two groups: projection- and reconstruction-based methods. In the projection-based methods, scatter correction is usually performed by subtracting the scatter contribution from the projection data before the actual reconstruction [1]. These methods differ in how the scatter contribution is determined. The projection-based methods are usually easy to implement and fast to execute, but the overall improvement in image quality achieved with the scatter compensation, is often reduced by the noise increase in the reconstructed images owing to the subtraction procedure. The reconstruction-based scatter-correction methods, on the other hand, include the effects of scatter into the forward- and backprojec-

tors of the reconstruction algorithm without direct scatter subtraction. The reconstruction-based methods have been shown to achieve greater accuracy and lower noise level than the projection-based methods [2, 3], but they are often unsuitable for clinical practice owing to unacceptably long execution times because scatter calculations have to be repeated at each iteration of the reconstruction algorithm.

One promising projection-based scatter-correction method that has received a lot of attention is the transmission-dependent convolution subtraction (TDCS) algorithm [4]. TDCS has been used by our group to correct scatter in cerebral blood flow [5] and dopamine transporter [6] quantitation studies. Despite the relatively good performance of TDCS in the aforementioned experiments, TDCS is still hampered by the fact that as a projection-based scatter-correction method it relies on scatter subtraction, and also by the fact that it needs geometric mean (GM) projection data, which for example renders accurate collimator-blurring correction impossible.

Even though the traditional TDCS scatter correction has its limitations, the transmission-dependent scatter-modeling approach, when included in reconstruction-based scatter-compensation method, might prove to be useful. Hutton et al. [7, 8] used transmission-dependent scatter modeling to generate scatter projections, which could be included in iterative reconstruction algorithm to perform reconstruction-based scatter compensation in their two-step reconstruction procedure. In this method, Hutton first reconstructed a "scatter-free" image using broad-beam attenuation map. This image was then used as an input for a transmission-dependent scatter-modeling algorithm to calculate scatter projections, which were finally used as a constant additive term in the final "scatter-corrected" reconstruction according to the method of Bowsher and Floyd [9]. The objective of our work was to extend the two-step transmission-dependent scatter correction by Hutton to a "more natural" single-step scatter-compensation method and to include it into a fast 3D reconstruction algorithm with attenuation and collimator-blurring corrections. We also compared our new reconstruction method with Hutton's method and also with conventional TDCS scatter-correction approach in terms of quantitative accuracy, contrast, and image quality.

Materials and methods

Implementation of the reconstruction algorithms

The attenuation, collimator blurring, and scatter correction were implemented into ordered subsets expectation

maximization (OSEM) algorithm [10]. The OSEM is given by

$$f_j^{new} = \frac{f_j^{old}}{\sum_{i \in S_n} a_{ij}} \sum_{i \in S_n} a_{ij} \frac{p_i}{\sum_k a_{ik} f_k^{old}}, \tag{1}$$

where f is the reconstructed image, p the measured projections, j (or k) reconstruction voxel index, i projection pixel index, a_{ij} the probability that emission from voxel j is detected in pixel i, and S_n the nth subset. The image update in OSEM consists of sequential forward- and backprojection operations. The estimated projections are obtained by forwardprojecting the current image estimate ($\sum_k a_{ik} f_k^{old}$) and correction terms that are used to update the old image are formed by backprojecting the ratio of the measured and estimated projections

$(\sum_{i \in S_n} a_{ij} \frac{p_i}{\sum_k a_{ik} f_k^{old}})$.

Here, the forward- and backprojectors were implemented as rotation based [11] (Fig. 1a), which makes attenuation, collimator blurring, and scatter correction relatively straightforward to perform. Attenuation correction factors for each voxel were calculated simply by summing the rotated attenuation map along columns. Collimator blurring, on the other hand, was modeled by convolving each plane of the reconstruction matrix parallel to the projection plane with a collimator response kernel, which was spatially invariant in that plane (Fig. 1b) [12]. The collimator response function was assumed to be a 2D Gaussian function, whose full width at half maximum (FWHM) is linearly dependent on the distance (d_{col}) from the plane to the collimator

$$FWHM(d_{col}) = \alpha + \beta d_{col}. \tag{2}$$

Scatter modeling was implemented by slightly modifying the method presented by Hutton et al. [7, 8]. Hutton's method applies the rotating projectors and it compensates scatter as follows:

1. At each projection angle a "scatter-free" image, which has been obtained with reconstruction of the measured projection data using broad-beam attenuation coefficients, is first multiplied with monoexponential scatter kernel ($e^{-\alpha(d_{tis})r}$), whose slope (α) is dependent on depth (d_{tis}) in tissue. A single scatter kernel is used for each plane at different tissue depth (see Fig. 1b).

2. Each point on each plane is then scaled with a transmission-dependent scatter-to-primary scatter fraction $SF_{S/P}$:
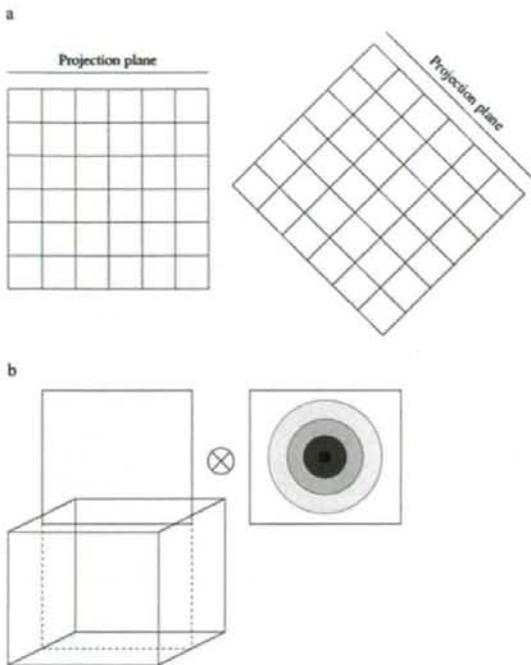
a

b

Fig. 1 a At each projection angle (two projection angles are shown), the rotating projector rotates the reconstruction matrix (single transverse plane is shown) so that its front face is aligned with the projection plane. The projections can be calculated simply by summing along columns of the reconstruction matrix. **b** Collimator response and scatter response modeling are realized by convolving each plane of the rotated reconstruction matrix (3D view is shown) parallel to the projection plane with an appropriate kernel

$$SF_{S/P} = A - B \left[e^{-\sum_{k=j}^{skin} \mu_k \Delta} \right]^\gamma - 1, \qquad (3)$$

where A, B, and γ are the coefficients obtained from measurement [4], μ_k is the linear attenuation coefficient for voxel k and Δ voxel size.

3. The convolved and scaled voxel values are finally forwardprojected for obtaining scatter projection for the current projection angle.
4. After all the scatter projections are available, a new reconstruction is started. In this final reconstruction, the scatter projections obtained in the previous step are held as a constant term (s), which is added to the calculated projections $\left(\sum_k a_{ik} f_k^{old} + s \right)$.

Our new method differs from Hutton's method by the fact that it does not use a pre-reconstructed broad-beam attenuation coefficient image to calculate the scatter

projections, but instead we perform the convolution and scatter-fraction scaling using the current image estimate (f_j^{old}). Therefore, our scatter compensation can be presented as

1. In the forwardprojection step of the OSEM algorithm at each projection angle the current image estimate (f_j^{old}) is convolved with the scatter kernels.
2. Each point on each plane is then scaled with the transmission-dependent scatter fraction.
3. The convolved and scaled voxel values are finally forwardprojected and added to the forwardprojected primary counts.

We believe that our approach leads to more natural scatter compensation, reduces user intervention and execution time.

Scatter modeling makes reconstruction time consuming and therefore we used coarse-grid modeling [13] to provide further improvement in speed. In coarse-grid scatter modeling, scatter compensation is performed using larger voxel size than the actual reconstruction voxel size (in our case scatter was calculated using a 64 × 64 × 64 matrix in the case of a 128 × 128 × 128 reconstruction matrix). It is also worth pointing out that our method models scatter only in the forwardprojection step and do not use collimator-blurring compensation in scatter estimation.

The conventional TDCS was implemented according to Meikle et al. [4] using a single exponential convolution kernel and scatter-to-total scatter fractions ($SF_{S/T}$)

$$SF_{S/T} = \frac{1}{A - Bt_i^{\beta/2}}, \qquad (4)$$

where t_i is transmission factor for projection pixel i. Convolution with the depth-independent scatter kernel ($e^{-\alpha r}$) was performed to the measured projections (p_{meas}) after taking the GM and the result was scaled with the scatter fraction. The resulting scatter projections were subtracted from the measured projections for obtaining "scatter-free" projections (p_{nosc}):

$$p_{nosc} = p_{meas} - SF_{S/T}(p_{meas} \otimes e^{-\alpha r}). \qquad (5)$$

The scatter-free projections were finally reconstructed using OSEM.

Reconstruction algorithm calibration

The parameters needed for collimator blurring and scatter correction were obtained from Monte Carlo simulations with the SIMIND simulator [14]. A low-energy
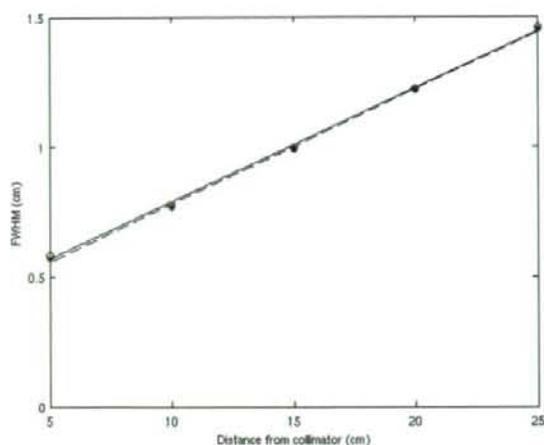
Fig. 2 Full width at half maximum as a function of distance from the collimator for ^{99m}Tc and ^{123}I. ^{99m}Tc measurements are shown with *circles* and the linear model fit (Eq. 2) as *solid line*, whereas ^{123}I measurements are presented with *stars* and the linear model fit as *dashed line*. The parameters α and β in Eq. 2 for ^{99m}Tc were 0.35 and 0.04 and for ^{123}I 0.33 and 0.04, respectively

Fig. 3 Scatter kernel slope as a function of depth in water for ^{99m}Tc and ^{123}I. ^{99m}Tc measurements are shown with *solid line* with *circles* and ^{123}I measurements using *dashed line* with *stars*

high-resolution parallel hole collimator with 0.14 cm in hole diameter, a hole length of 2.7 cm, and a septal thickness of 0.018 cm was used. The pixel size in the simulations was set to 0.2 cm, and the projection data were acquired into a 128×128 matrix. Two sets of simulations were performed using ^{99m}Tc and ^{123}I as radionuclides. Symmetrical 15% energy window was centered on the photo-peak. For ^{123}I high-energy photons were not included in the simulations.

The FWHM as a function of distance was obtained by simulating point sources in air at different distances (5 cm, 10 cm, 15 cm, 20 cm, and 25 cm) from the collimator. FWHM was calculated by fitting a Gaussian function to a profile drawn through the center of the image, and the intercept (α) and slope (β) in Eq. 2 were obtained by fitting the linear model to the measurements (see Fig. 2).

The scatter kernel slope $[\alpha(d_{tis})]$ for the reconstruction-based scatter-correction methods (Hutton's method and new method) was obtained by simulating a line source behind slabs of different thickness (2 cm, 4 cm, 6 cm, 8 cm, 10 cm, 12 cm, 14 cm, 16 cm, 18 cm, and 20 cm) of water. Low noise level planar images of the line sources were acquired and the slopes were calculated by fitting exponential functions to the scatter tails of profiles drawn through the center of the image. The results of this experiment are presented in Fig. 3. The slope for each plane at different depths in tissue in the reconstruction-based scatter correction was obtained by linear interpolation from the measurements. The slope for depth-indepen-
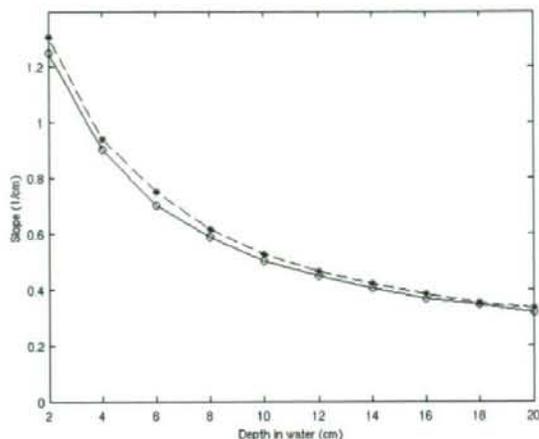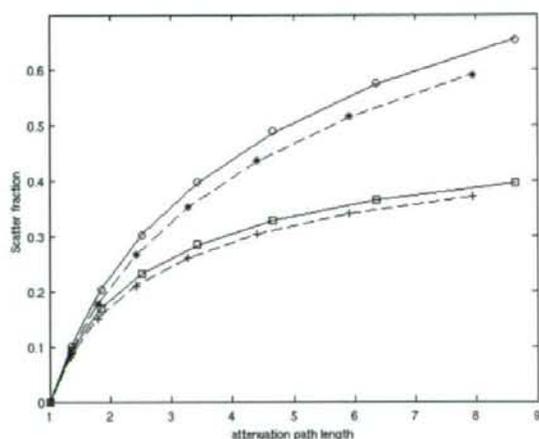

Fig. 4 Scatter fractions as a function of attenuation path length for ^{99m}Tc and ^{123}I. Scatter-to-primary ^{99m}Tc measurements are shown with *circles*, scatter-to-primary ^{123}I measurements with *stars*, scatter-to-total ^{99m}Tc measurements with *squares*, and scatter-to-total ^{123}I measurements are presented with *plusses*. The build-up equation fit (Eqs. 3, 4) for ^{99m}Tc is shown with *solid line* and for ^{123}I as *dashed line*. The build-up equation parameters A, B, and γ were 3.6, 2.6, and 0.13 for ^{99m}Tc and 4.3, 3.3, and 0.09 for ^{123}I. The same A, B, and γ parameters fitted well in both Eqs. 3 and 4

dent scatter kernel in the conventional TDCS was set to 0.45 l/cm for ^{99m}Tc and 0.47 l/cm for ^{123}I.

The A, B, and γ scatter-fraction coefficients were calculated by simulating point sources behind slabs of different thicknesses (2 cm, 4 cm, 6 cm, 8 cm, 10 cm, 12 cm, and 14 cm) of water. The scatter fractions were obtained from SIMIND, and these measurements were

fitted to Eqs. 3 and 4. Results from this experiment are presented in Fig. 4.

Brain phantom simulations

The new reconstruction-based scatter-correction method was compared with that of Hutton's method and to TDCS using the Zubal brain phantom [15]. The phantom was modified to represent the uptake of ^{99m}Tc-ECD (gray-to-white matter ratio 2.5:1) and ^{123}I-FP-CIT (striatum-to-background ratio 4:1). SIMIND was used to create low noise projection data of the phantoms, 120 angles over 360° circular orbit, by simulating approximately 70 MCts/projection using the same parameters as was used in determining the parameters for the reconstruction algorithms with the exception that pixel size was now 0.225 cm. Attenuation map was created by assigning correct densities for brain tissue and skull. The low-noise projections were then used to create noisy projection sets containing a total of 5 MCts for the ^{99m}Tc-ECD and 2 MCts for the ^{123}I-FP-CIT, which represent the average total count levels of ^{99m}Tc-ECD and ^{123}I-FP-CIT in clinical studies (personal communication Prof. Jyrki T. Kuikka, Kuopio University Hospital, Finland).

The noisy projection data were reconstructed using the new algorithm with (4 iterations and 15 subsets) and without collimator modeling (2 iterations and 15 subsets) and the GM projections with/without TDCS (2 iterations and 10 subsets). Reconstructions with collimator modeling used more iterations because of their slower convergence. Both reconstructions according to Hutton's method were performed with 2 iterations and 15 subsets. All the reconstructed images were post-filtered using a 3D Butterworth filter (cut-off 1.0 cycles/cm, order 5) according to clinical practice. The accuracy of the reconstruction methods was studied by comparing the overall accuracy of the reconstruction and correction methods and by calculating the normalized mean-

squared error (NMSE) with respect to the known true counts (f_j^{true}):

$$NMSE = \frac{\sum_j (f_j^{true} - f_j)^2}{\sum_j f_j^{true2}}$$ (6)

and the average gray-to-white matter and striatum-to-background ratios.

Results

Results of the Zubal brain phantom experiments are shown in Table 1. As can be seen, the reconstruction-based scatter-correction methods outperform the conventional TDCS in terms of contrast (gray-to-white matter and striatum-to-background ratios) and quantitative accuracy (normalized mean-squared errors). The new method is more accurate than that of Hutton's one, but the difference between the two is small. Highest accuracy is achieved when collimator-blurring correction is also applied during reconstruction. Indeed, collimator-blurring compensation might prove to be very useful in quantitative brain studies because it clearly reduces the partial volume effect offering higher accuracy. Interestingly, reconstructions from GM projections with only attenuation correction perform worse than reconstructions from normal projections. This is primarily caused by differences in attenuation correction. GM projections require projection space attenuation correction, whereas more accurate reconstruction space attenuation correction can be performed with normal projections. Examples of images with different reconstruction methods are shown in Figs. 5 and 6. The reconstruction-based scatter-compensation methods provide slightly better image quality than TDCS and the best result is obtained when collimator-blurring correction is also applied.

Table 1 Normalized mean-squared error (NMSE), gray-to-white matter ratio (GM:WM), and striatum-to-background ratio (STR:BG) for the ^{99m}Tc-ECD and ^{123}I-FP-CIT simulation studies

Corrections	NMSE$_{ECD}$	GM:WM	NMSE$_{FP-CIT}$	STR:BG
Attenuation^a	0.186/0.182	1.11/1.17	0.136/0.134	2.19/2.24
Attenuation + scatter$_{TDCS}$	0.179	1.15	0.134	2.27
Attenuation + scatter$_{Hutton}$	0.173	1.24	0.127	2.29
Attenuation + scatter$_{New}$	0.172	1.25	0.126	2.29
Attenuation + scatter$_{New}$ + CDR	0.165	1.41	0.121	2.48

Results are presented for ordered subsets expectation maximization (OSEM) reconstruction with only attenuation correction, with attenuation and scatter correction [transmission-dependent convolution subtraction (TDCS)-based, Hutton's method and new method] and with attenuation, new scatter, and collimator-blurring correction (CDR). The attenuation correction only results are presented for two algorithms: geometric mean (GM) projection OSEM reconstruction, which has to be used for TDCS-based scatter correction and normal OSEM reconstruction which is used for Hutton's and new scatter-compensation methods
^{a} The first values shown are the results of GM projection reconstruction and the second the results of normal reconstruction
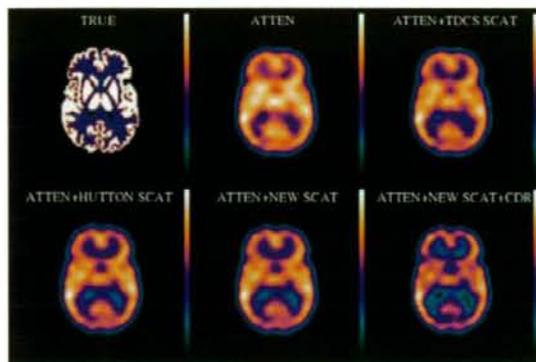
Fig. 5 Representative slices of the ⁹⁹ᵐTc-ECD study obtained with ordered subsets expectation maximization (OSEM) using only attenuation correction (reconstruction with normal projections), attenuation + transmission-dependent convolution subtraction (TDCS)-based scatter correction, attenuation + Hutton's scatter correction, attenuation + new scatter correction, and attenuation + new scatter + collimator-blurring (CDR) correction
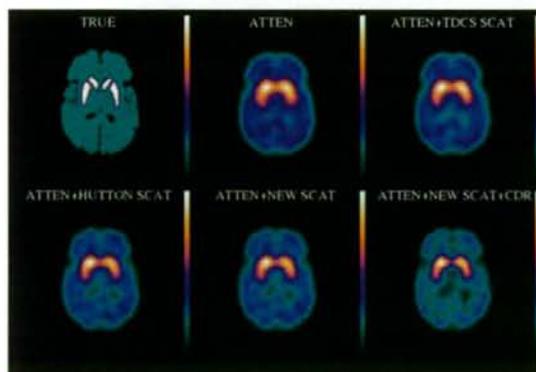
Table 2 Average reconstruction times for the ⁹⁹ᵐTc-ECD and ¹²³I-FP-CIT studies

Corrections	Time per iteration (s)
Attenuation[a]	67/212
Attenuation + scatter$_{TDCS}$	67
Attenuation + scatter$_{Hutton}$[b]	560 + 212
Attenuation + scatter$_{New}$	254
Attenuation + scatter$_{New}$ + CDR	336

Results are presented for OSEM reconstruction with only attenuation correction, with attenuation and scatter correction (TDCS-based, Hutton's method and new method) and with attenuation, new scatter, and collimator-blurring correction (CDR). The attenuation correction only results are presented for two algorithms: geometric mean (GM) projection OSEM reconstruction, which has to be used for TDCS-based scatter correction and normal OSEM reconstruction which is used for Hutton's and new scatter-compensation method. Calculation times have been obtained using 1.7 GHz Pentium processor with 1 GB RAM
[a] The first value shown is the time for GM projection reconstruction and the second is for normal reconstruction
[b] Pre-reconstruction and scatter forwardprojection calculation time + time for single iteration for the final reconstruction

Fig. 6 Representative slices of the ¹²³I-FP-CIT study obtained with OSEM using only attenuation correction (reconstruction with normal projections), attenuation + TDCS-based scatter correction, attenuation + Hutton's scatter correction, attenuation + new scatter correction, and attenuation + new scatter + CDR correction

The average reconstruction times of the ⁹⁹ᵐTc-ECD and ¹²³I-FP-CIT Zubal phantom experiments are listed in Table 2. The TDCS is much faster than other methods, but it is worth noting that because of the GM projections TDCS uses only 60 projections in reconstruction, whereas the new method uses 120 projection images. TDCS also applies projection-based attenuation modeling as explained earlier, and therefore it does not require rotation of the attenuation map during the reconstruction, which saves time. Hutton's method is by far the slowest one because it requires pre-reconstruction to cal-

culate scatter projections, but when the scatter projections are ready the actual scatter correction in the final reconstruction is faster than scatter compensation with the new method.

Discussion

Here, we implemented a 3D reconstruction algorithm with transmission-dependent scatter modeling for efficient reconstruction-based scatter correction and compared it with reconstruction-based scatter-compensation method presented by Hutton et al. [7, 8], and with the conventional TDCS-based scatter-correction method [4]. The new algorithm proved to provide the highest accuracy according to Monte Carlo simulation studies of Zubal brain phantom (see Table 1). The new algorithm is also very advantageous because it allows easy incorporation of accurate attenuation and collimator-blurring corrections, which might prove to be very useful in high-quality SPECT imaging.

The presented scatter-correction method is relatively easy to implement and use. It requires two measurements for calibration: line source measurement to determine the scatter kernel slopes and point source measurement to determine the scatter fractions. These measurements need to be performed once for each radionuclide and collimator pair. In fact for lower-energy isotopes such as ⁹⁹ᵐTc, the scatter fractions have shown to be collimator independent [16] and therefore a single measurement might be sufficient for scatter-correction calibration for a large family of different collimators.

In addition to the ease of implementation, the execution time is of importance if a reconstruction method is to be used in clinical practice. Table 2 lists the calculation times per iteration for the scatter-correction methods. The TDCS-based scatter correction is clearly the fastest method, but the new method does not provide an extensive increase in computation time when compared with reconstruction without scatter correction. It is worth pointing out that even though the new method was accelerated using the coarse-grid scatter modeling, the reconstruction algorithm itself is not yet fully optimized. We believe that by further optimizing the structure of our reconstruction code and by replacing the current bilinear interpolation-based reconstruction grid rotation with a faster three-pass shear [17] method, we can still greatly reduce the computation time from the current 336 s/iteration.

This study has some limitations. First, testing and comparison of algorithms was performed using simplified simulated data. Simulated data were chosen, because they allowed easy comparison with true activity distributions, which are beneficial to finding small errors in initial reconstruction experiments. Simulations were performed as Monte Carlo simulations, which are known to have relatively good correspondence with real clinical data and we also tried to closely mimic clinical-imaging situations using appropriate noise levels and post-filters. On the other hand, it should be realized that even Monte Carlo simulations will probably produce results that are too good owing to the absence of errors in energy window calibration, non-uniformities, and so on that often hamper the quality of clinical data. Moreover, the high-energy photons of ^{123}I, which can penetrate or scatter at the collimator, were not included in the simulations, and the reconstructions were performed with noise-free and perfectly aligned attenuation maps. Both of these conditions are unnatural and their effects have to be investigated in detail in further studies.

Second, the metrics (NMSE and activity ratios) that were used to analyze the reconstructed images are simplistic, and more clinically relevant measures such as cerebral blood flow, binding potential, or task-based measures such as lesion detection are required in future studies to evaluate the true benefits of the presented reconstruction and corrections methods. Comparison of the new transmission-dependent scatter correction with other reconstruction-based scatter-correction methods such as in Beekman et al. [18] and Frey et al. [19] would also make an interesting topic for a further investigation.

In summary, we have proposed a 3D reconstruction algorithm with attenuation, collimator blurring, and transmission-dependent scatter correction, which shows promise as an efficient and accurate reconstruction method; however, further testing is still required to evaluate its true applicability in the clinical setting.

References

1. Buvat I, Rodriguez-Villafuerte M, Todd-Pokropek A, Benali H, Di Paola R. Comparative assessment of nine scatter correction methods based on spectral analysis using Monte Carlo simulations. J Nucl Med 1995;36:1476–88.
2. Frey EC, Tsui BMW, Ljungberg M. A comparison of scatter compensation methods in SPECT: subtraction-based techniques versus iterative reconstruction with accurate modeling of the scatter response. Conference Record of the 1992 Nuclear Science Symposium and Medical Imaging Conference 1992;2:1035–7.
3. Beekman FJ, Kamphuis C, Frey EC. Scatter compensation methods in 3D iterative reconstruction: a simulation study. Phys Med Biol 1997;42:1619–32.
4. Meikle SR, Hutton BF, Bailey DL. A transmission-dependent method for scatter correction in SPECT. J Nucl Med 1994;35:360–7.
5. Iida H, Narita Y, Kado H, Kashikura A, Sugawara S, Shoji Y, et al. Effects of scatter and attenuation correction on quantitative assessment of regional cerebral blood flow with SPECT. J Nucl Med 1998;39:181–9.
6. Kim KM, Varrone A, Watabe H, Shidahara M, Fujita M, Innis RB, et al. Contribution of scatter and attenuation compensation to SPECT images of nonuniformly distributed brain activities. J Nucl Med 2003;44:512–9.
7. Hutton BF, Osiecki A, Meikle SR. Transmission-based scatter correction of 180° myocardial single-photon emission tomographic studies. Eur J Nucl Med 1996;23:1300–8.
8. Hutton BF, Baccarne V. Efficient scatter modelling for incorporation in maximum likelihood reconstruction. Eur J Nucl Med 1998;25:1658–65.
9. Bowsher JE, Floyd CE. Treatment of Compton scattering in maximum-likelihood expectation maximization reconstructions of SPECT images. J Nucl Med 1991;32:1285–91.
10. Hudson HM, Larkin RS. Accelerated image reconstruction using ordered subsets of projection data. IEEE Trans Med Imaging 1994;13:601–9.
11. Zeng GL, Gullberg GT. Frequency domain implementation of the three-dimensional geometric point response correction in SPECT imaging. IEEE Trans Nucl Sci 1992;39:1444–53.
12. Zeng GL, Gullberg GT, Bai C, Christian PE, Trisjono F, Di Bella EVR, et al. Iterative reconstruction of fluorine-18 SPECT using geometric point response correction. J Nucl Med 1998;39:124–30.
13. Kadrmas DJ, Frey EC, Karimi SS, Tsui BMW. Fast implementations of reconstruction-based scatter compensation in fully 3D SPECT image reconstruction. Phys Med Biol 1998;43:857–73.
14. Ljungberg M, Strand SE. A Monte Carlo program for the simulation of scintillation camera characteristics. Comput Methods Programs Biomed 1989;29:257–72.
15. Zubal IG, Harrell CR, Smith EO, Rattner Z, Gindi G, Hoffer PB. Computerized three-dimensional segmented human anatomy. Med Phys 1994;21:299–302.

16. Kim KM, Watabe H, Shidahara M, Ishida Y, Iida H. SPECT collimator dependency of scatter and validation of transmission-dependent scatter compensation methodologies. IEEE Trans Nucl Sci 2001;48:689–96.

17. Di Bella EVR, Barclay AB, Eisner RL, Schafer RW. A comparison of rotation-based methods for iterative reconstruction algorithms. IEEE Trans Nucl Sci 1996;43:3370–6.

18. Beekman FJ, de Jong HW, van Geloven S. Efficient fully 3-D iterative SPECT reconstruction with Monte Carlo-based scatter compensation. IEEE Trans Med Imaging 2002;21: 867–77.

19. Frey EC, Ju ZW, Tsui BMW. A fast projector-backprojector pair modeling the asymmetric, spatially varying scatter response function for scatter compensation in SPECT imaging. IEEE Trans Nucl Sci 1993;40:1192–7.